Electronic Supplementary Material (ESI) for Nanoscale.


# Supporting Information

# Shape-dependent Thermo-plasmonic Effect of Nanoporous gold at the Nanoscale for Ultrasensitive Heat-mediated Remote Actuation

Zhe Yang[a,#], Xuemei Han[a,#], Hiang Kwee Lee[a,b,#], Gia Chuong Phan-Quang[a], Charlynn Sher Lin Koh[a], Chee Leng Lay[a,b], Yih Hong Lee[a], Yue-E Miao[c], Tianxi Liu[c], In Yee Phang[b,#], Xing Yi Ling[a,*]

[a] Division of Chemistry and Biological Chemistry, School of Physical and Mathematical Sciences, Nanyang Technological University, 21 Nanyang Link, Singapore 637371.

[b] Institute of Materials Research and Engineering, Agency for Science, Technology and Research (A*STAR), 2 Fusionopolis Way, Innovis, #08-03, Singapore 138634.

[c] State Key Laboratory for Modification of Chemical Fibers and Polymer Materials, College of Materials Science and Engineering, Donghua University, Shanghai 201620, P.R. China.

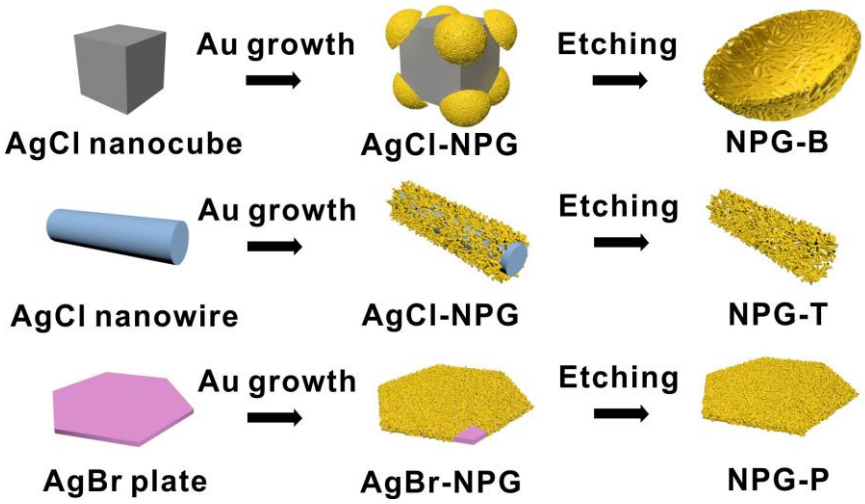


**Figure S1.** Scheme for the synthesis of nanoporous gold with bowl-like (NPG-B; top), tube-like (NPG-T; middle) and plate-like (NPG-P; bottom) structures.

The elaborated formation mechanism of nanoporous gold nanoparticles on Ag halide-based sacrificial template, such as nanoprous gold bowls, has been reported in our previous work.[1,2] Briefly, the NPG formation undergoes two steps. First, heterogeneous Au nucleation occurs on the surface of existing AgCl seeds and continual growth of Au into nanoporous gold (NPG) structure. This is followed by removal of AgCl templates with $NH_4OH$ to yield standalone NPG. We used polyvinylpyrrolidone (PVP) as surfactant for NPG growth, which also functions as a pore-forming agent due to their strong absorption on the growing Au surface.[3] For nanowire- and plate-shaped sacrificial template, Au nucleate selectively on the outer surface of respective Ag salts because of their large surface area as well as high and homogeneous surface free energy. Au continuously grow from the nuclei and along the Ag templates to yield the corresponding NPG-T and NPG-P. On the other hand, Au nanoparticles selectively nucleate on the sharp corners and edges of cube-shaped AgCl seeds due to their comparatively higher surface free energy. Owing to the huge lattice mismatch on cubic AgCl seeds, Au nanoparticles grow exclusively on the Au nuclei rather than conformally along the Ag template to form the resultant NPG-B.

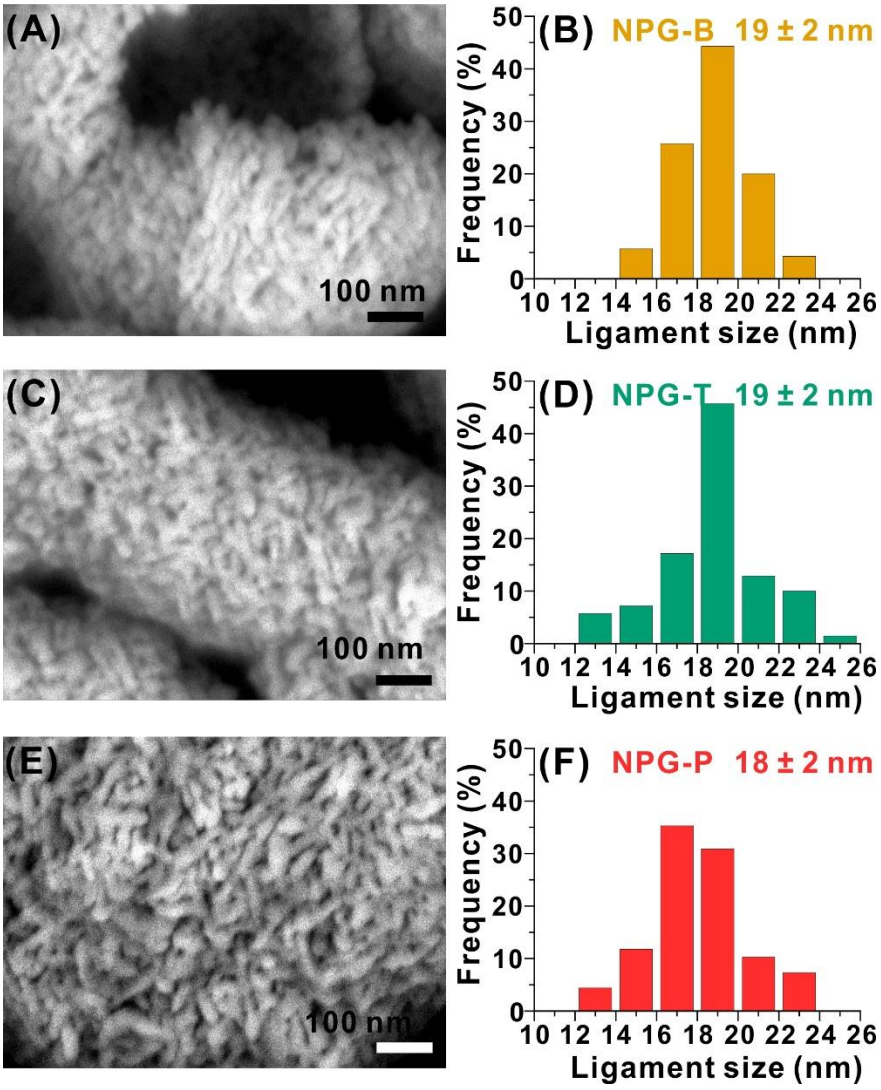


**Figure S2**. Magnified SEM images and corresponding ligament size distributions of (A, B) NPG-B, (C, D) NPG-T and (E, F) NPG-P.

The pore size distribution of NPG-B, NPG-T, and NPG-P in this work are largely determined from the magnified SEM images (Figure S2) of respective NPG structures. In these images, we clearly see the unique structures of various NPGs which contain randomly-distributed pore with pore size ranging from 4 to 30 nm. This finding is in close agreement to our previous work,[1] whereby pore sizes of NPG-B (ligament size ~ 20 nm) synthesized using the exact protocol were determined to be in the range of 3-20 nm using Brunauer-Emmett-Teller (BET) $N_2$ adsorption evaluation.

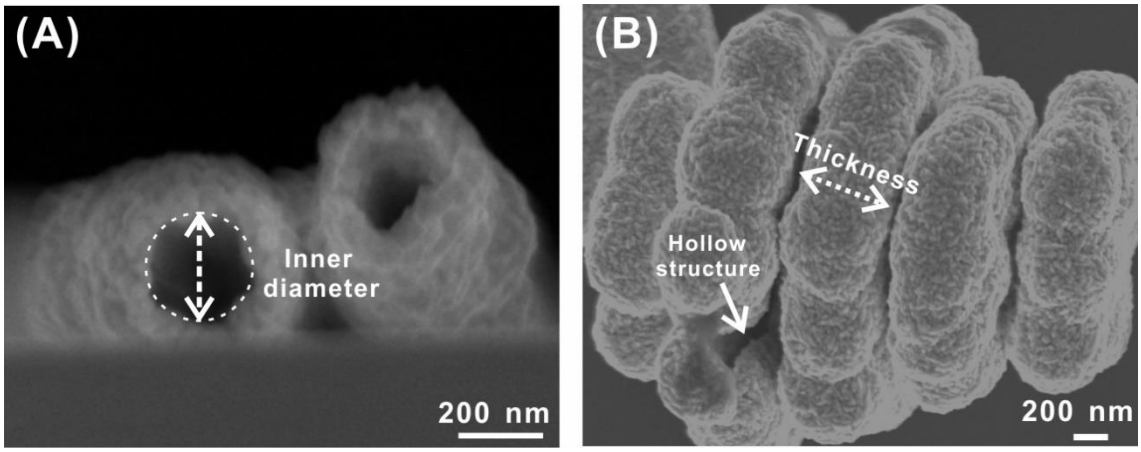


**Figure S3**. (A) Cross-sectional SEM image of NPG-T. The dotted circle indicate the inner diameter of hollow NPG tube. (B) SEM images of NPG-P. The dotted arrow denotes the thickness of NPG-P. The solid arrow indicate the hollow structure of NPG-P.

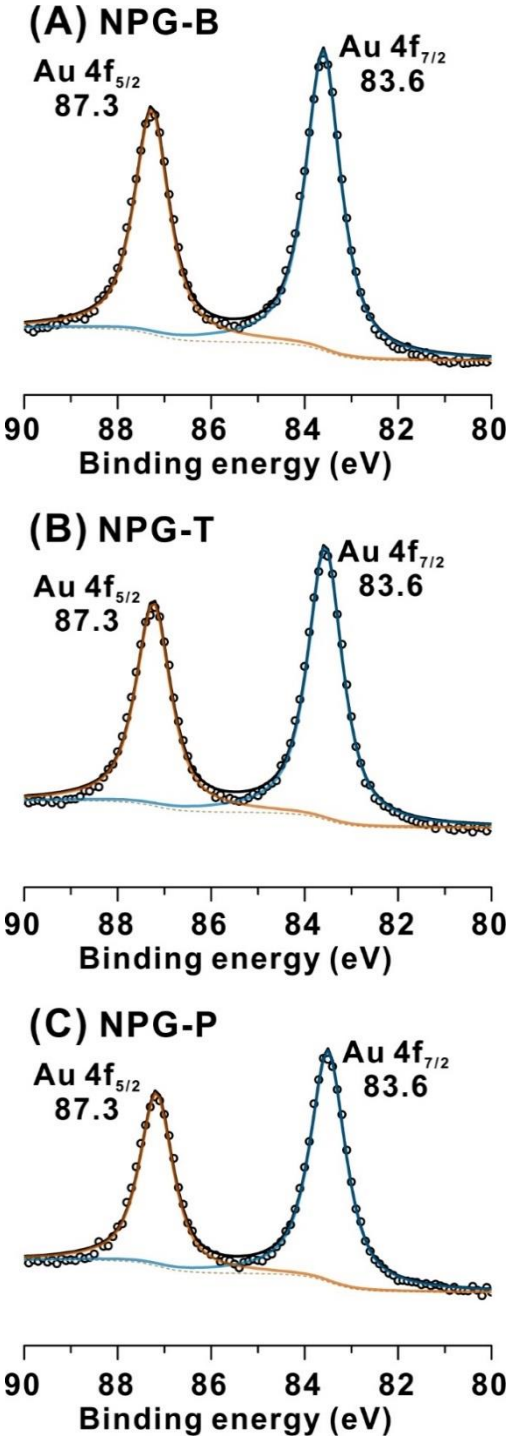


**Figure S4.** XPS of Au in (A) NPG-B, (B) NPG-T and (C) NPG-P.

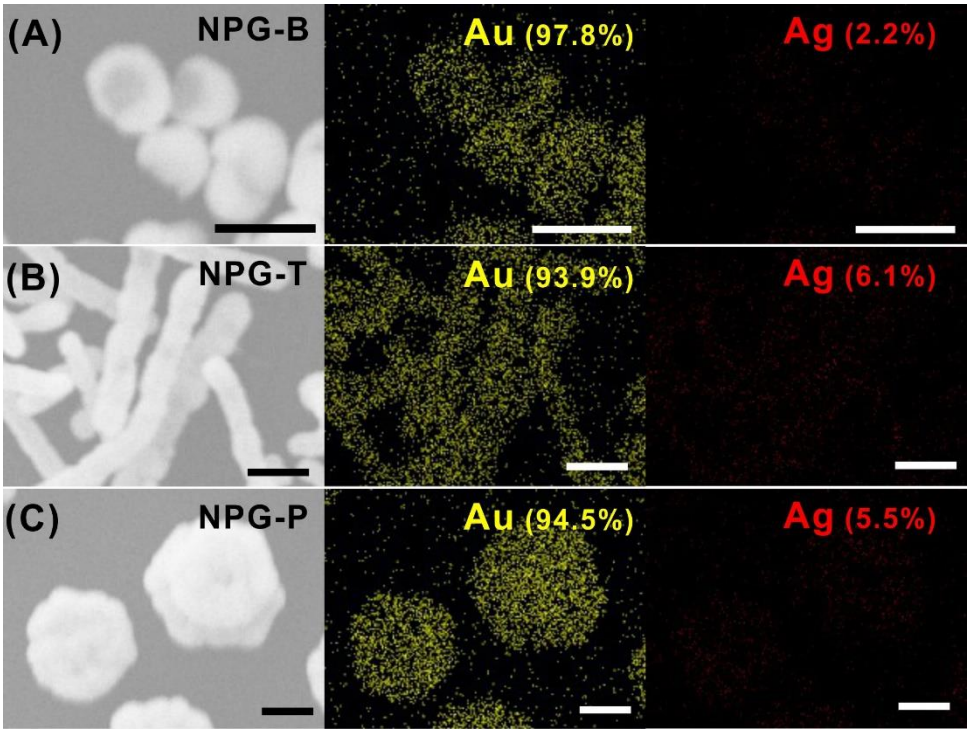


**Figure S5.** SEM images and their corresponding EDS mapping of (A) NPG-B, (B) NPG-T and (C) NPG-P. Scale bars, 1 μm.

**Table S1**. The weight and atom ratio of Ag determined using inductively coupled plasma optical emission spectrometry (ICP-OES) analysis on as-synthesized NPG-B, NPG-T, and NPG-P.

| **NPG shapes** | **Ag / (Ag + Au)** **wt%** | **Ag / (Ag + Au)** **atom%** |
|---|---|---|
| NPG-B | 1.88 ± 0.01 | 3.38 ± 0.01 |
| NPG-T | 2.14 ± 0.00 | 3.83 ± 0.00 |
| NPG-P | 3.18 ± 0.01 | 5.66 ± 0.02 |

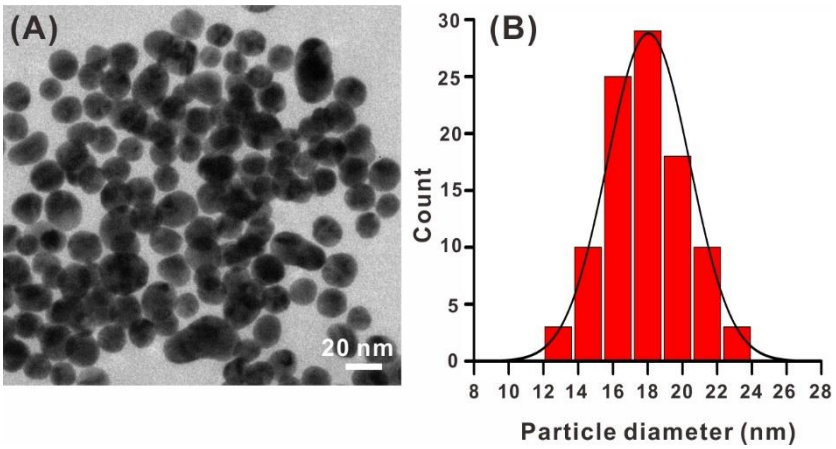


**Figure S6.** (A) TEM image of as-synthesized Au nanoparticles and their (B) size distribution with an average particle diameter of (18 ± 2) nm.

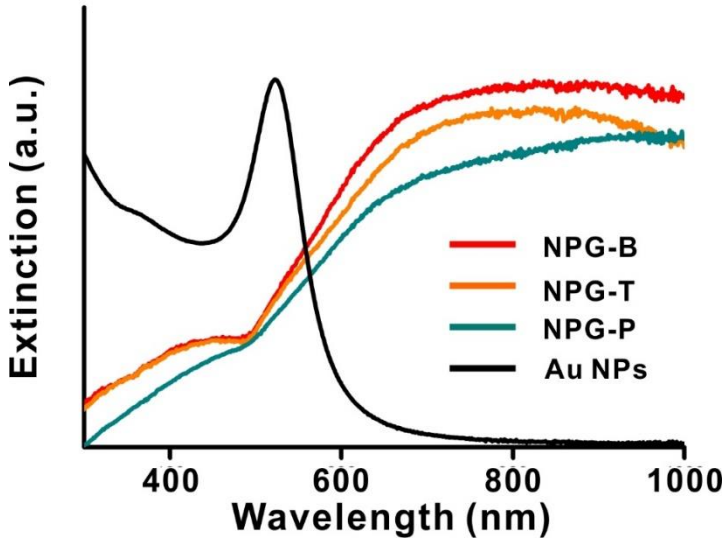


**Figure S7.** UV-vis spectra of NPG-B, NPG-T and NPG-P, as well as Au nanoparticles with average size of 18 nm in diameter.

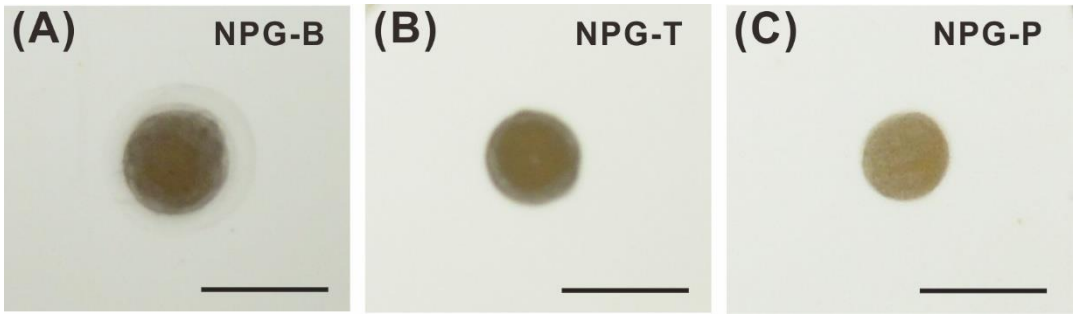


**Figure S8.** Digital images of (A) NPG-B, (B) NPG-T, and (C) NPG-P deposited on TLC substrates. Scale bars, 5 mm.

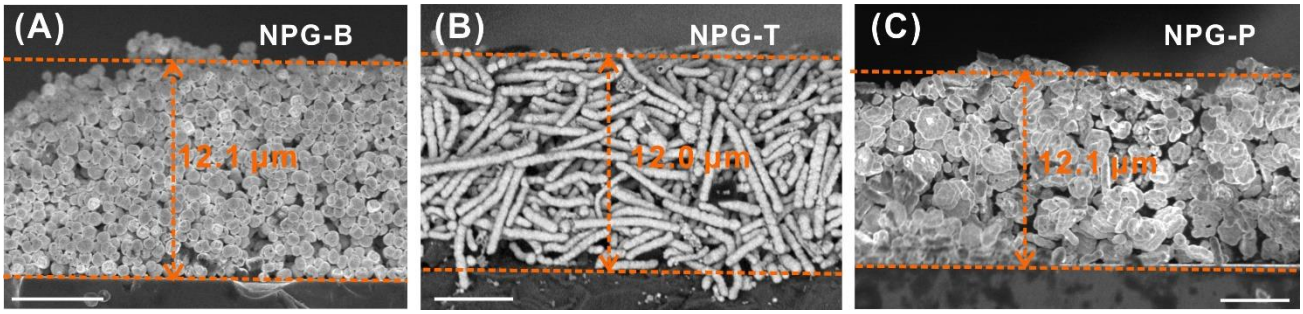


**Figure S9.** Cross-sectional SEM images and corresponding thickness of (A) NPG-B, (B) NPG-T and (C) NPG-P. Scale bars, 5μm.

The layer thickness of the NPG-B layer is estimated to be 12 μm from the cross-sectional SEM image (Figure S9A). Based on NPG-B's average size of 0.7 μm, the estimated layer of NPG-B is ~ 17 layers.

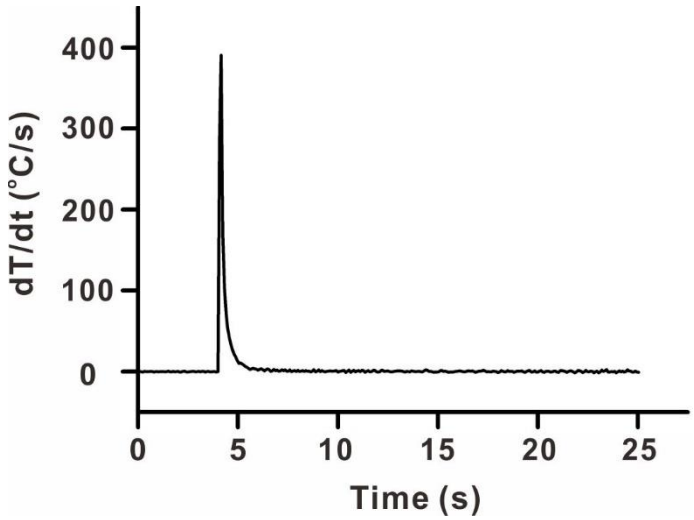


**Figure S10.** Heating speed of NPG-B under irradiation of 90 mW laser.

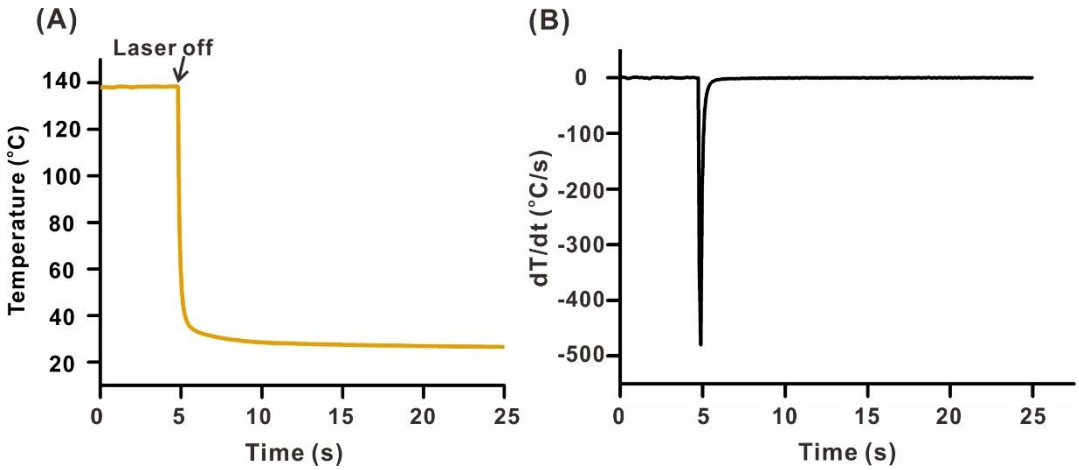


**Figure S11.** (A) Temperature-time profiles of the central irradiated zone of NPG-B when the irradiation laser is switched off. (B) 1$^{st}$ derivative of (A) which represents the cooling speed of the central irradiated zone of NPG-B.

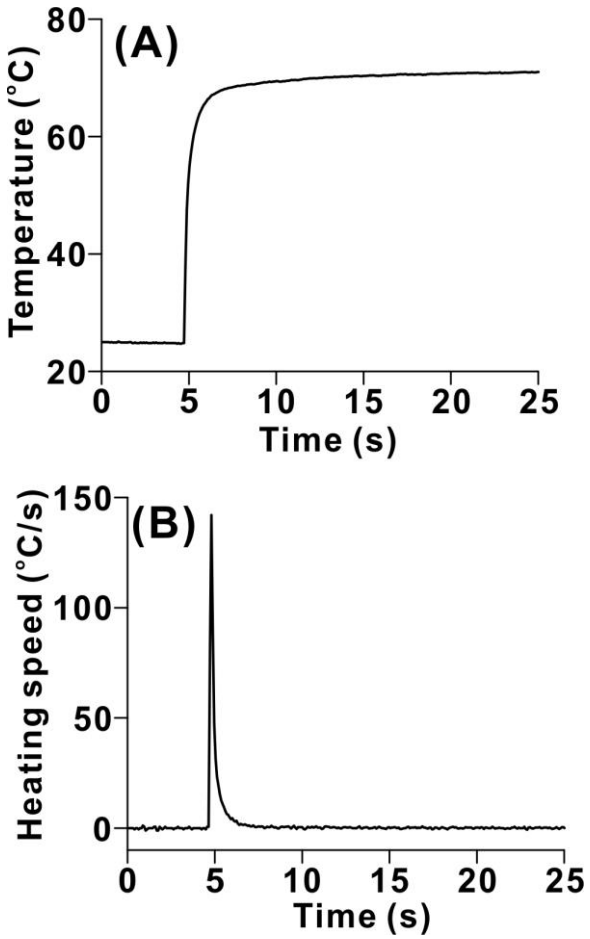


**Figure S12.** (A) Temperature-time profile of the central irradiated zone of Au nanoparticles deposited on TLC plate when the irradiation laser is switched on. (B) 1$^{st}$ derivative of (A) which represents the temperature changing rate of the central irradiated zone of Au nanoparticles.

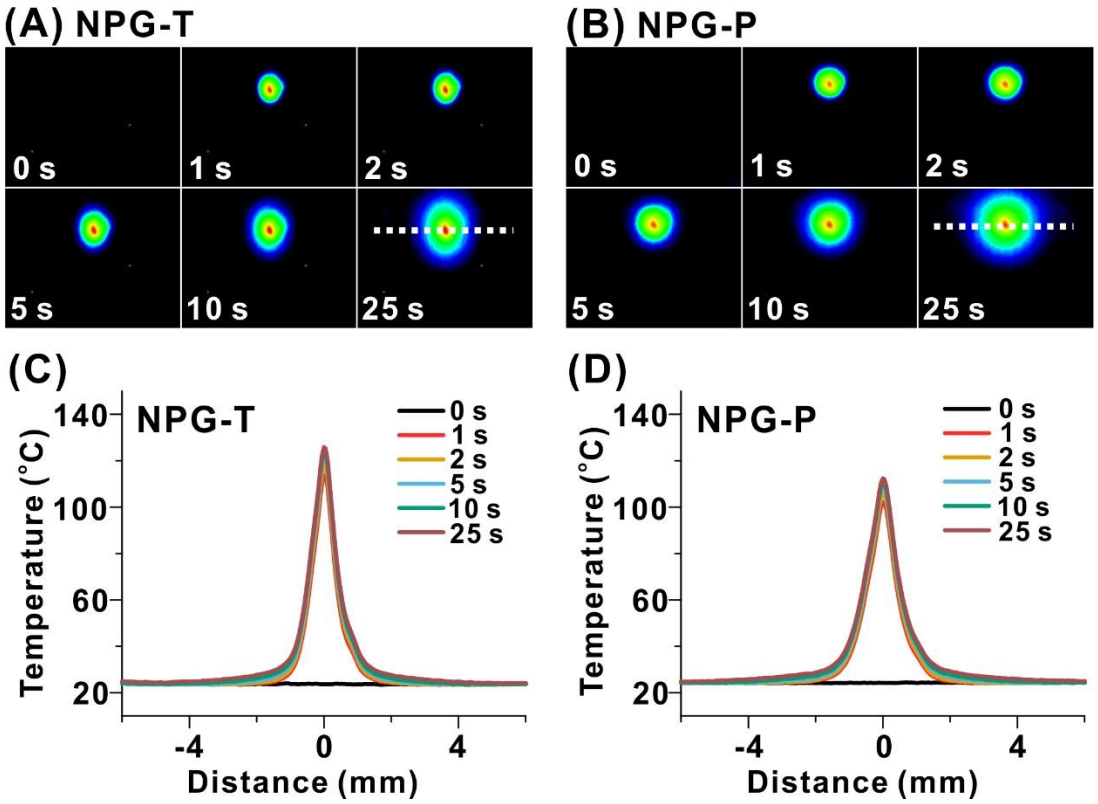


**Figure S13.** Thermograms and corresponding spatial temperature profiles of (A, C) NPG-T and (B, D) NPG-P when the irradiation laser is switched on.

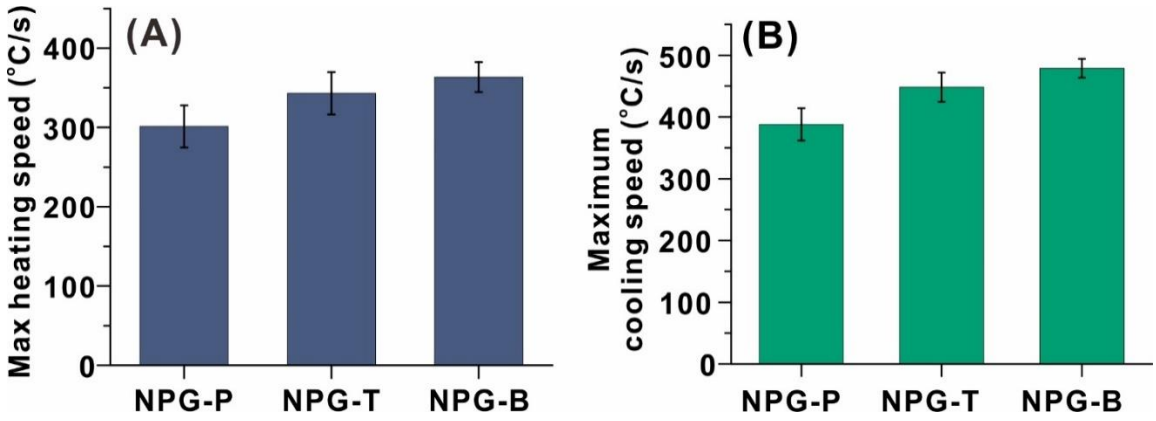


**Figure S14.** Comparison of the (A) maximum heating speed and (B) cooling speed of NPG-B, NPG-T, and NPG-P.

**Supporting Notes 1:** Calculation of apparent photothermal conversion efficiency

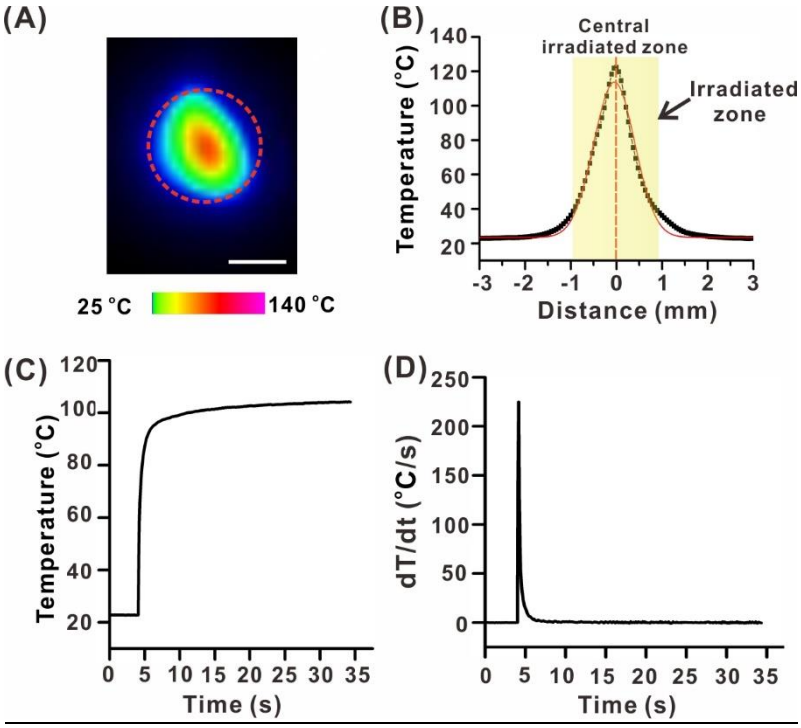


**Figure S15.** (A) Thermogram of NPG-B at 1s after switching on the laser at a power of 89.1 mW and (B) corresponding Gaussian-fitted spatial temperature distribution on the horizontal line across central irradiated zone. Scale bar in (A), 1 mm. (C) Temperature-time profiles of irradiated area (within the red ring) during photothermal heating. (D) 1st derivative curve of (C), showing the temperature increasing rates (dT/dt) within the overall irradiated zone. Temperature in (C) and (D) refer to the average temperature achieved within the irradiated zone.

The photothermal conversion process is analyzed by employing a theoretical model based on energy balance of NPG layers under laser irradiation. Photothermal conversion efficiency ($\eta$) is used to quantitatively evaluate the capability of converting the laser into thermal energy and determined using equation S1:[4]

$$\eta = \frac{Q}{E} = \frac{Cm\Delta T}{Pt} \qquad \text{(S1)}$$

where $Q$ denotes the photogenerated thermal energy and is calculated using heat capacity ($C$) and mass ($m$) of material as well as the temperature increment ($\Delta T$) during laser irradiation. $E$ denotes the energy of incident laser and is determined from the power of laser ($P$) and irradiation time ($t$).

Generally, we observe that the localized temperature of NPG layers increased rapidly in the initial period of irradiation, followed by a temperature equilibrium even with continued laser irradiation

(Figure 2D; Figure S15C). Due to the Gaussian laser beam applied in the experiment, 95% of energy conversion occurred within the dotted circle area with a radius of 0.85 × FWHM = 1.0 mm (Figure S15A),[5] where FWHM = 1.2 mm is obtained with the Gaussian equation (highlighted area in Figure S15B). Hence, NPG layer within this area is utilized as the overall irradiated zone for determination of the photothermal conversion efficiency.

Considering that we directly deposited NPG onto TLC plate, the heat capacity from both NPG ($C_{Au}$, 0.126 J $g^{-1}$ $K^{-1}$) and silica gel layer ($C_{silica}$, 0.921 J $g^{-1}$ $K^{-1}$)[6] were used for the calculation of $Q$ according to the first law of thermodynamics ($Q = Cm\Delta T$).[7]

Typically, for NPG-B, the mass of NPG-B and silica gel within the circle ring (irradiated zone) can be estimated to be 23.7 and 267 μg, respectively, according to the apparent mass density of NPG-B (7.55 μg/$mm^2$) and silica gel (85 μg/$mm^2$) determined using ICP-OES.

The rate of average temperature change in the irradiated area, $\Delta T/t$, can be determined from the $dT/dt$ at the moment of triggering the laser (Figure S15C and S15D).

$$\Delta T/t = dT/dt = 244\ ^{o}C/s$$

The laser power is experimentally measured to be 89.1 mW. Using equation S1, the photothermal conversion efficiency of NPG-B under laser irradiation is thus estimated to be:

$$\eta = \frac{(C_{Au} \times m_{Au}) + (C_{silica} \times m_{silica})}{P} \times \frac{\Delta T}{t}$$

$$= \frac{[(0.126 \times 23.7) + (0.921 \times 267)] \times 10^{-6}}{89.1 \times 10^{-3}} \times 244 \times 100\%$$

$$= 68\%$$

Similarly, the photothermal conversion efficiency of NPG-T, NPG-P, Au nanoparticles and smooth Au nanoplate are calculated and listed in Table S2.

**Table S2.** Photothermal efficiency of NPG-B, NPG-T, NPG-P, Au nanoparticles, and smooth Au nanoplates.

| Sample | Photothermal conversion efficiency |
|---|---|
| NPG-B | (68 ± 2)% |
| NPG-T | (56 ± 5)% |
| NPG-P | (49 ± 2)% |
| Au nanoparticles | (29 ± 4)% |
| Au nanoplates | (10 ± 1)% |

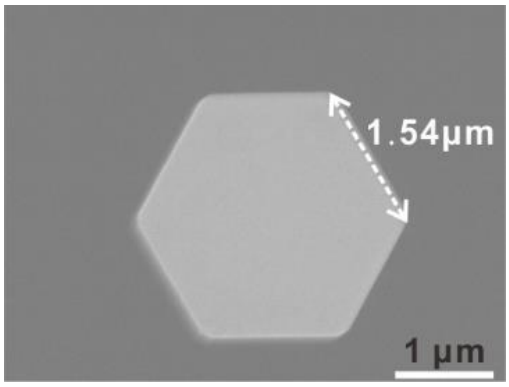


**Figure S16.** SEM image of smooth Au nanoplate. The dotted arrow denotes the edge length of Au nanoplate with an estimated average length of 1.54 μm.

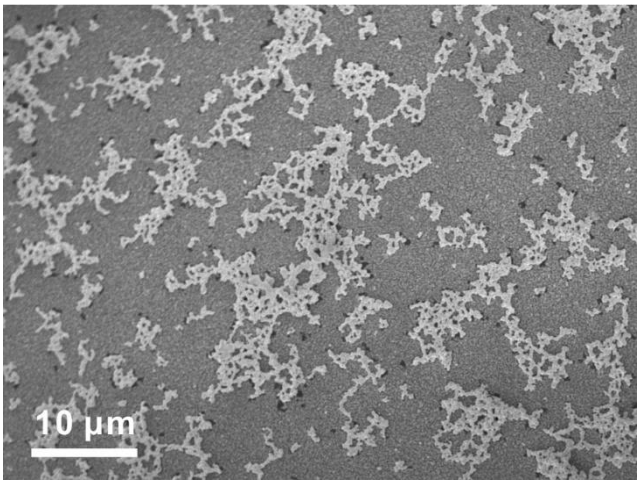


**Figure S17.** SEM image of Au nanoparticles clusters deposited on Si substrate.

**Supporting Notes 2:** Calculation of absorption cross section ($C_{abs}$)

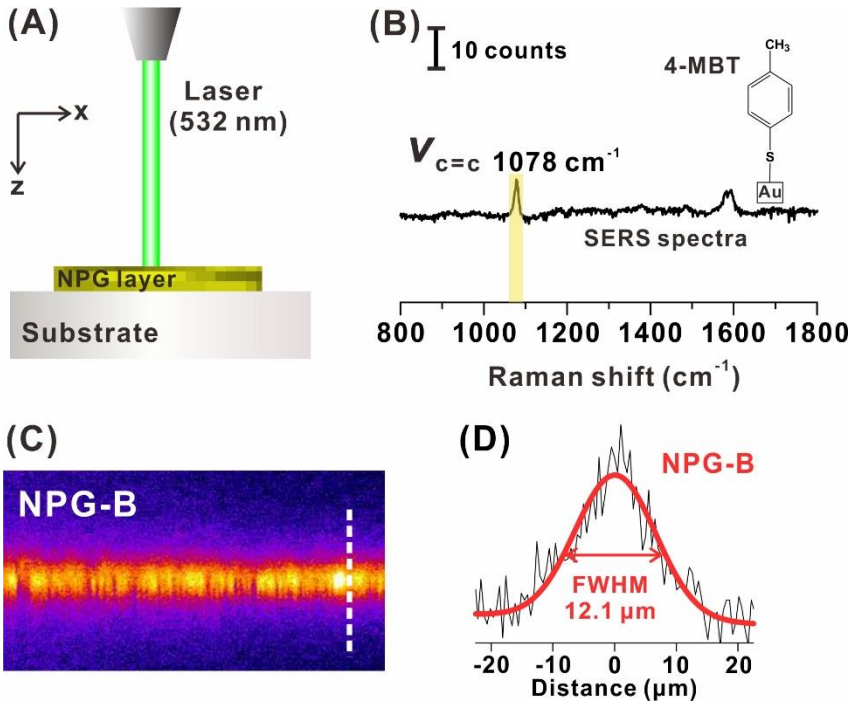


**Figure S18.** (A) Scheme illustrating the hyperspectral surface-enhanced Raman spectroscopy (SERS) imaging of NPG particle cluster. (B) SERS profile of 4-MBT grated on NPG-B. The inset displays the molecule structure of 4-MBT functionalized Au surface. (C) X-z SERS image and its (D) corresponding intensity line profile. The white solid line denote the location at which the intensity line profile is obtained, from the upperside to the underside of these particle clusters.

Absorption cross section ($C_{abs}$) of NPG, which measures the ability of a material to absorb a photon upon light irradiation, can be calculated using the following equation S2:[4]

$$C_{abs} = \frac{Q}{d \times N \times P \times \Delta t} \qquad \text{(S2)}$$

where $Q$ is the heat generated during laser irradiation, $d$ is laser penetration depth, $N$ is the apparent density of nanoporous gold (g/m$^3$), $P$ is the laser power, $\Delta t$ is time.

The apparent density of nanoporous gold ($N$), can be calculated as:

$$N = \frac{m_{Au}}{A \times d} \qquad \text{(S3)}$$

where $m_{Au}$ is the mass of NPG that effectively interact with laser; A is the laser spot area.

The previously discussed photothermal conversion efficiency, $\eta$, can be calculated as:

$$\eta = \frac{Q}{E} = \frac{Q}{Pt} \qquad \text{(S4)}$$

Combining equation S2, S3 and S4, the absorption cross section can be derived as,

$$C_{abs} = \frac{\eta}{m_{Au}} \times A \qquad \text{(S5)}$$

The laser spot area is previously estimated to be 3.14 $mm^2$ in Supporting Notes 1. To determine $C_{abs}$ more representatively, we only consider the mass of NPG-B that can effectively absorb light because only these particles will be able to subsequently convert such photon energy into heat energy. The effective mass of NPG-B can be in turn estimated by measuring the effective laser penetration depth (*d*) using hyperspectral surface-enhanced Raman spectroscopy (SERS) imaging (Figure S18A). In this method, a monolayer of 4-methylbenzenethiol (MBT) is grafted onto the NPG surfaces as a SERS probe. When exposed to excitation irradiation, these probe molecules will undergo Raman scattering and their intensity-distance profiles along the z-axis (into the depth of particle cluster) are commonly employed to yield critical information on laser penetrability;[8,9] only topmost particle layers directly exposed to excitation laser will undergo Raman scattering. From the SERS spectra, we observe unique MBT's phenyl-ring stretching vibrational modes centered at 1078 $cm^{-1}$ (Figure S18B). X-z SERS imaging of NPG-B reveals a FWHM of 12.1 μm obtained with the Gaussian equation (Figure S18C and S18D). The resolution in z direction of the Nanophoton system is estimated to be 8.5 μm.[9] Thus the effective laser penetration depth (*d*) for NPG-B layer is determined to be 1.699 × (12.1 - 8.5) = 6.1 μm. Using a previously-determined NPG-B density of 7.55 μg/$mm^2$, we therefore calculate the effective mass of NPG-B ($m_{Au}$) that interact with laser as followed:

$$m_{Au} = 7.55 \times 3.14 \times (6.1 / 12.1) = 11.85 \text{ μg}$$

(note that the thickness of the entire particle cluster is 12.1 μm as demonstrated in Figure S9A.

Thus, the $C_{abs}$ of NPG-B is calculated according to equation S5 as followed:

$$C_{abs} = (0.68 \times 3.14) / 11.85$$
$$= 0.18\ mm^2/\mu g$$
$$= 1.8 \times 10^5\ mm^2/g$$

Similarly, we calculate and summarize the $C_{abs}$ for NPG-P, NPG-T, and AuNPs in Figure 2F. More importantly, we also note that the AuNPs with particle size similar to NPG's ligament have a calculated $C_{abs}$ of $1.1 \times 10^5\ mm^2/g$, corresponding to a $C_{abs}$ of $1.4 \times 10^{-17}\ m^2$ per nanoparticle. Our $C_{abs}$ value is notably comparable with theoretical prediction using Mie theory ($10^{-17}$-$10^{-16}\ m^2$ for gold nanoparticles with particle size range of 10-20 nm) as well as experimental results from previous literatures (~$2\times10^{-16}\ m^2$, size of 15 nm),[4,10,11,12] thus affirming that the assumptions and calculation methods proposed in our case are rationale for the determination of $C_{abs}$.

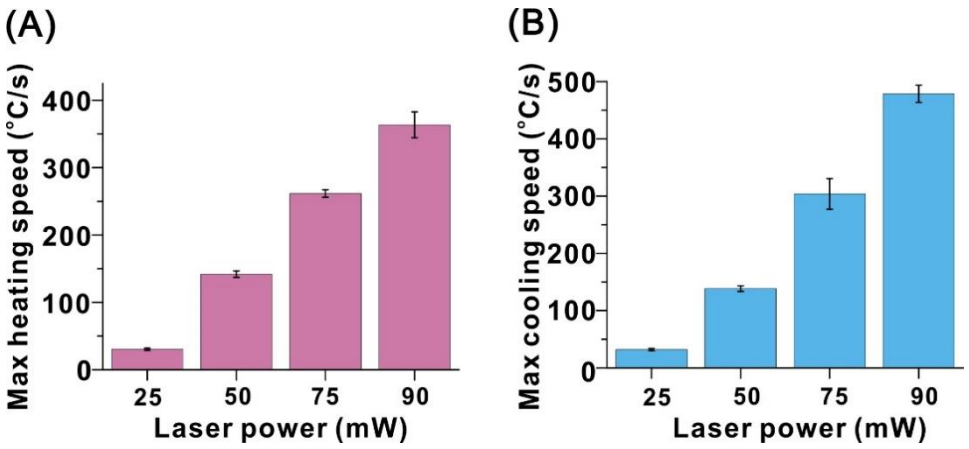


**Figure S19.** (A) Maximum heating speed and (B) maximum cooling speed of NPG-B when laser power is regulated between 25 and 90 mW.

**References**


1. Pedireddy S., Lee H. K., Koh C. S. L., Tan J. M. R., Tjiu W. W. and Ling X. Y., *Small*, **2016**, *12*, 4531-4540.

2. Pedireddy S., Lee H. K., Tjiu W. W., Phang I. Y., Tan H. R., Chua S. Q., Troadec C. and Ling X. Y., *Nat. Commun.*, **2014**, *5*, 4947.

3. W. Chen, Y. Su, L. Zhang, Q. Shi, J. Peng and Z. Jiang, *J. Membrane Sci.*, 2010, 348, 75-83.

4. Qin, Z.; Wang, Y.; Randrianalisoa, J.; Raeesi, V.; Chan, W. C. W.; Lipinski, W.; Bischof, J. C. *Sci. Rep.* **2016**, *6*, 29836.

5. Podzimek, S. *Light scattering, size exclusion chromatography and asymmetric flow field flow fractionation: powerful tools for the characterization of polymers, proteins and nanoparticles*; John Wiley & Sons, 2011.

6. Ng, K.; Chua, H.; Chung, C.; Loke, C.; Kashiwagi, T.; Akisawa, A.; Saha, B. *Appl. Therm. Eng.* **2001**, *21*, 1631-1642.

7. Jiang, K.; Smith, D. A.; Pinchuk, A. *J. Phys. Chem. C* **2013**, *117*, 27073-27080.

8. Adar, F.; Lee, E.; Mamedov, S.; Whitley, A. *Microsc. Microanal*. **2010**, *16*, 361.

9. Lee, H. K.; Lee, Y. H.; Phang, I. Y.; Wei, J.; Miao, Y.-E.; Liu, T.; Ling, X. Y. *Angew. Chem. Int. Ed.* **2014**, *53*, 5054-5058.

10. Jain, P. K.; Lee, K. S.; EI-Sayed, I. H.; EI-Sayed, M. A. *J. Phys. Chem. B*, **2006**, *110*, 7238-7248.

11. Chen, Y. S.; Frey, W.; Kim, S.; Homan, K.; Kruizinga, P.; Sokolov, K.; Emeliganov, S. *Opt. Express*. **2010**, *18*, 8867-8878.

12. Fong, K. E.; Yung, L. Y. L. *Nanoscale*, **2013**, *5*, 12043-12071.